Heat flux analysis of Type-I ELM impact on a sloped, protruding surface in the JET bulk tungsten divertor

(Article begins on next page)
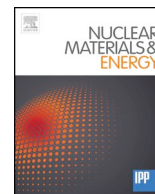
21 December 2024

Heat flux analysis of Type-I ELM impact on a sloped, protruding surface in the JET bulk tungsten divertor

J. Gaspar[a],*, J.W. Coenen[c], Y. Corre[a], R. Dejarnac[b], M. Firdaouss[a], F. Clairet[a], J. Gunn[a], D. Iglesias[d], M. Komm[b], K. Krieger[e], G. Matthews[d], R.A. Pitts[f], S. Silburn[d], JET contributors[#]

[a] *CEA Cadarache, F-13108 St Paul lez Durance, France*
[b] *Institute of Plasma Physics, Czech Academy of Sciences, 182 00 Prague, Czech Republic*
[c] *Forschungszentrum Jülich GmbH, Institut für Energie- und Klimaforschung – Plasmaphysik, 52425 Jülich, Germany*
[d] *CCFE, Culham Science Centre, Abingdon, OX 14 3DB, UK*
[e] *Max-Planck-Institut f. Plasmaphysik, Boltzmannstr. 2, D-85748 Garching, Germany*
[f] *ITER Organisation, Route de Vinon-sur-Verdon, CS 90 046, F-13067 St Paul-lez-Durance cedex, France*

ABSTRACT

Tungsten (W) melting due to transient power loads, for example those delivered by edge localised modes (ELMs), is a major concern for next step fusion devices. A series of experiments has been performed on JET to investigate the dynamics of Type-I ELM-induced transient melting. Following initial exposures in 2013 of a W-lamella with sharp leading edge in the bulk W outer divertor, new experiments have been performed in 2016–2017 on a protruding W-lamella with a 15° slope, allowing direct and spatially resolved (0.85 mm/pixel) observation of the top surface using the IR thermography system viewing from the top of the poloidal cross-section. Thermal and IR analysis have already been conducted assuming the geometrical projection of the parallel heat flux on the W-lamellas, thus ignoring the gyro-radius orbit of plasma particles. Although it is well justified during L-mode or inter-ELM period, the hypothesis becomes questionable during ELM when the ion Larmor radius is larger. The goal of this paper is to extend the previous analysis based on the forward approach to the H-mode discharges and investigate in particular the gyro-radius effect during the Type-I ELMs, those used to achieve transient melting on the slope of the protruding W-lamella. Surface temperatures measured by the IR camera are compared with reconstructed synthetic data from 3D thermal modelling using heat loads derived from optical projection of the parallel heat flux (ignoring the gyro-radius orbit), 2D gyro-radius orbit and particle-in-cell (PIC) simulations describing the influence of finite Larmor-radius effects and electrical potential on the deposited power flux. Results show that the ELM power deposition behaves differently than the optical projection of the parallel heat flux, contrary to the L-mode observations, and may thus be due to the much larger gyro-orbits of the energetic ELM ions in comparison to L-mode or inter-ELM conditions.

1. Introduction

ELM-induced transient melting is a major concern for ITER tokamak and also next step fusion devices. If the ELM power density is sufficiently high, the surface temperature can exceed the melting point for W and melt layer can be, partially or totally, removed. A series of experiment have been performed in the frame of ITPA multi-device activity in support to ITER [1] on JET [2–4], AUG [5], COMPASS [6], KSTAR [7] and DIII-D [8] to study carefully the leading edge loading, melting dynamic and also to investigate the consequences for plasma operation.

By virtue of its size, the amplitude of unmitigated Type-I ELMs on JET can be sufficient to induce transient melting at the divertor target plates. A first experiment was performed in JET in 2013 using a special lamella with a sharp leading edge gradually varying from $h = 0.25$ mm to 2.5 mm in the poloidal direction towards the high field side in order to maximise the inter-ELM temperature rise [2,3]. Moving the outer strike point onto the sharp leading edge for about 1 s enabled to reach an inter-ELM surface temperature higher than 2500 °C allowing transient, ELM-induced melting during the subsequent duration of the pulse. ELM-induced repetitive transient melting has been successively achieved for a series of 7 very reproducible plasma discharges with
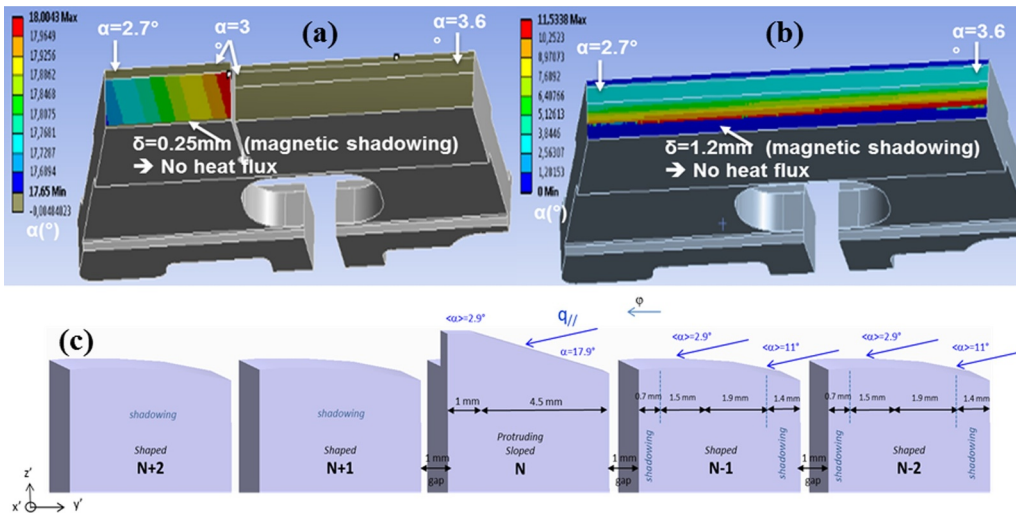
Fig. 1. Angle between magnetic field lines with top surfaces computed with the PFCflux software (#91965 @ $t = 12$ s), on sloped (a) and shaped (b) lamella respectively. The magnetic shadowing from the previous lamella is found to be about $\delta = 1.2$ mm on the shaped lamella. (c) Schematic view of the protruding sloped lamella and shaped lamellas as well as the direction of the incoming plasma flux and the incident angle.

plasma current of 3 MA and input power of 23 MW. However IR data analysis performed on both, reference and special lamellas, revealed significant discrepancies. The heat flux computed on the vertical side face was indeed found to be lower by a factor of 2 in H-mode and of 5 in L-mode compared to geometrical consideration. Using the available IR viewing geometry from top vertically down to the target plate surface, it was not possible to directly discriminate between the top and leading edge power loads.

Following initial exposures in 2013 of a W-lamella with sharp leading edge, new experiments have been performed in 2016–2017 on a protruding W-lamella with a 15° slope, allowing direct and spatially resolved (0.85 mm/pixel) observation of the top surface using the IR thermography system viewing from the top of the poloidal cross-section [4]. The new geometry results in a smaller temperature gradient compared to that on the top surface of the leading edge sample and correspondingly reduced sensitivity to the magnetic field incidence angle, permitting improved derivation of the incoming parallel heat flux in comparison to the sharp leading edge. Analysis based on the forward approach using the full 3D heat load and thermal modelling of the lamellas has already been performed assuming optical projection of the parallel heat flux on the lamella surface, together with a specific IR correction to account for effects related to spatial resolution [9]. Using the same parallel heat flux, good agreement was obtained for three different geometries (sharp leading edge, protruding and standard lamellas) under L-mode conditions, validating the optical heat load projection assumption [10] with background (non-parallel) heat flux less of 1% of the parallel heat flux. A second methodology based on inverse analysis of the top surface temperature has been developed and applied to L-mode and H-mode plasma conditions [11]. Surface load reconstruction are performed with the inverse thermal code ALICIA based on simplified 2D geometries of the W-lamella (2D rectangular section) with geometrical correction to account for the shape and 3D geometry of the W-lamella, together with extremely fine finite element mesh in the plasma facing surface in order to capture ELM thermal dynamic. The main result obtained with the inverse methodology confirms the validity of the optical projection of the parallel heat flux as long as a non-constant and non-parallel heat flux component is considered (with non-parallel heat flux less of 1.2% and 1.9% of the parallel heat flux during L-mode and H-mode respectively when averaging inter-ELM and ELM loads).

During the ELM crash, the ion Larmor radius (r_L) becomes larger (>1mm) which is expected to modify particle and heat flux deposition as function of the geometry of the component. Numerical analysis based on PIC modelling has already been performed with the former sharp

leading edge W-lamella geometry [12]. On the misaligned side of the lamella which sees the direct parallel flux, the deposited power tends to be lower than the nominal value expected from geometric magnetic field line impact over a distance smaller than 2 Larmor radii. Using the available IR viewing geometry from the top of the poloidal cross-section, it was not possible to directly discriminate between the top and leading edge power loads and validate the numerical simulations. The goal of the work described here is to investigate the heat load during Type-I ELM, those used to achieve transient melting, on the slope of the protruding W-lamella allowing direct and spatially resolved (0.85 mm/pixel) observation of the top surface using the IR thermography system.

2. Experimental set-up and experiment description

2.1. Geometry of the standard and protruding lamella

The bulk tungsten divertor consists of lamellas assembled in four stacks named A, B, C and D, from the inner to the outer side of the torus. The lamellas are typically 40 mm high by 58 mm long by 5.5 mm wide with a toroidal gap of 1 mm [13]. The standard lamellas are shaped on the top surface in order to shadow their upstream edges from the parallel heat flux. The heat flux deposited on the shaped lamella is, therefore, non-uniform in both, toroidal (due to the variation of the inclination of the magnetic field line and magnetic shadowing) and poloidal (due to power decay length in the SOL and power spreading factor in the private flux region) directions respectively. The sloped special lamella is made up of a protruding 15° inclined surface, 20 mm long and 4.5 mm large, with a 1 mm flat top in order to avoid sharp corner. The rest of the lamella, on the outer side, is shaped identically to the standard ones. The protruding and shaped parts of the lamella are separated by a keyhole of 0.5 mm width and 10 mm depth. The keyhole behaves like a thermal barrier which separates the protruding from the standard parts of the lamella (strong discontinuity of temperature) this offers a clear advantage to validate the transfer function used to model the IR instrument. Fig. 1 shows the impact angle between the magnetic field lines and the surface of the lamellas for the pulse #91965. The 5 lamellas behind the sloped lamella are magnetically shadowed by the protruding part.

2.2. IR system

KL9A/B are two IR diagnostics dedicated to the study of temperatures and heat loads on the bulk tungsten divertor at two different toroidal locations, the protruding W-lamella being in the field of view

of the KL9A IR system [14]. The sampling frequency of the infrared camera can go up to 20 kHz depending on the size of the image frame and the spectral bandwidth is between 3.5 and 5 μm. The spatial resolution is determined by the optics and camera detectors. KL9B has a lens with a 100 mm focal length (*F/2*) while KL9A has a 200 mm focal length with the same *F*-number (i.e., *F/2*). Consequently, the spatial resolution of KL9A is higher (0.85 mm/pixel) than for KL9B (1.7 mm/pixel). The filter for KL9A is a low pass type centred at 4.2 ± 0.1 μm and for KL9B is a bandpass type centred at 3.9 ± 0.1 μm with a bandwidth of 1.6 μm. The emissivity of the tungsten is expected to vary linearly with temperature from 0.06 at 100 °C up to 0.23 at 3400 °C. The accuracy for temperature measurement due to camera noise, calibration errors and transmission responses has been evaluated to ± 50 °C [14].

For the pulse #91965 the sampling frequency are 2.5 and 9 kHz for KL9A and KL9B, respectively. The windowing of the IR view allows following 5 lamellas for KL9A and 3 lamellas for KL9B. For the rest of the paper the 5 lamellas seen by KL9A will be named "*N*" for the sloped lamella, "*N − 1*" and "*N − 2*" for the two upstream standard lamellas and "*N + 1*" and "*N + 2*" for the two downstream shadowed lamellas. One W-lamella will be study in the KL9B view and will named "standard".

2.3. Discharge description and ELMs statistical analysis

The transient melting of the sloped lamella, by regular Type-I ELMs, have been achieved during the H-mode pulse #91965 (3.25 MA/3.03 T with 27 MW input power) for *t* > 53 s [4]. Fig. 2(a) shows the maximum heating (*ΔT*) of the 5 lamellas measured by KL9A and one measured by KL9B for 38 ELMs counted in the 51.75–53 s time range. The measurements for the 3 shaped lamellas, those not affected by the sloped one on the upstream side, are consistent independently of the IR system (2 lamellas measured with KL9A and one with KL9B). The mean ELM temperature rise is ≈ 430 °C (with a standard deviation of ± 120 °C) and 210 °C (± 60 °C) for the protruding and standard lamella located on the upstream region respectively. The ratio of the heating between the shaped and the sloped lamellas is found to be 49 ± 9%. The ELM temperature rise reported on the downstream region, thus in the magnetically shadowed area is ≈ 55 °C (± 25 °C), which is about 20% of upstream non shadowed shaped lamellas heating. Such heating must be set against the accuracy of the temperature measurement at relatively low temperature on the shadowed lamella (about 400 °C) at very low emissivity of the tungsten which is prone to reflection from the hotter neighbouring W-lamella (1000 and 2000 °C for the standard shaped and sloped lamellas, respectively)

In order to study the heat load deposition on the different lamellas we select the ELM with the highest heating, Fig. 2(b), occurring at *t* = 12.048 s well before from when the melting occurs. The ELM duration is about 1 ms and 270 kJ of energy release (≈ 4.1% of W$_{plasma}$)

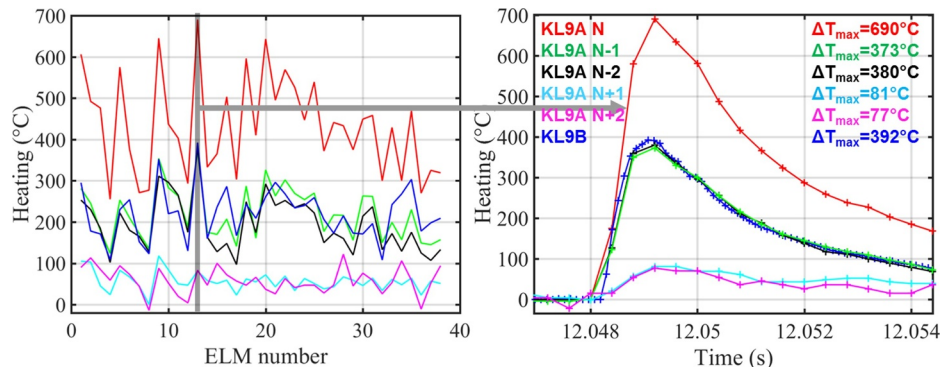determined with diamagnetic measurement. The comparison of the IR measurements done with KL9A (2.5 kHz) and KL9B (9 kHz) on the shaped lamellas shows similar ELM heating with KL9A despite the relative low sampling frequency comparing to the ELM duration (0.4 ms and 1.1 ms, respectively).

3. Heat load and heat transfer modelling

3.1. Optical projection

The optical projection comes from a purely geometrical point of view. Assuming plasma ions and electrons follow magnetic field lines with no consideration of Larmor gyration, electrical drift and collision with plasma particles, the heat load distribution can be computed with:

$$q_n = q_{\parallel} \times \sin(\alpha) + q_{BG} \tag{1}$$

where *α* is the impact angle between the magnetic field lines and the surface and q_{BG} represents the background heat flux (including plasma radiation and neutral particles coming from charge exchange) which is supposed here to be homogeneous for simplification. Fig. 1 shows the spatial distribution of the impact angle on the two lamellas for the pulse #91965 (@ *t* = 12 s).

3.2. Ion-orbit and PIC modelling

The particle and heat flux distribution can also be calculated by means of Particle-In-Cell (PIC) [15] or Ion-Orbit Codes (IOC) [16]. Each modelling has pros and cons for our study.

The ion-orbit modelling [16] takes into account the influence on the deposited power flux of finite Larmor radius effects associated with the energetic ELM. The code can handle the calculation on both the 15° slope and the round shaping of the standard W-lamella. The simulation box here is composed by the sloped lamella and 10 rounded lamella (with the rounded part approximated by several flat slopes).

The 2D-3V PIC code SPICE [15] can compute the deposited heat flux by including the Larmor radius effect as well as a self-consistent calculation of the sheath electric field which accelerate or slow-down the particles around any plasma-facing component. The limitation of the PIC modelling is about the geometry which can be modelled, up to now the round shaped lamella has not been yet investigated with this code. These lamellas are replaced by flat lamellas in the simulated box of the PIC calculations around the sloped lamella. The simulation box used here is composed by the sloped lamella and a long flat lamella upstream.

The input plasma parameters for the codes are electron and ion densities and temperatures measured at the top of the pedestal. Fig. 3 shows the density and temperature profiles measured with the High Resolution Thomson Scattering (HRTS) diagnostic before the ELM crash. The values of electron density and temperature are reported at
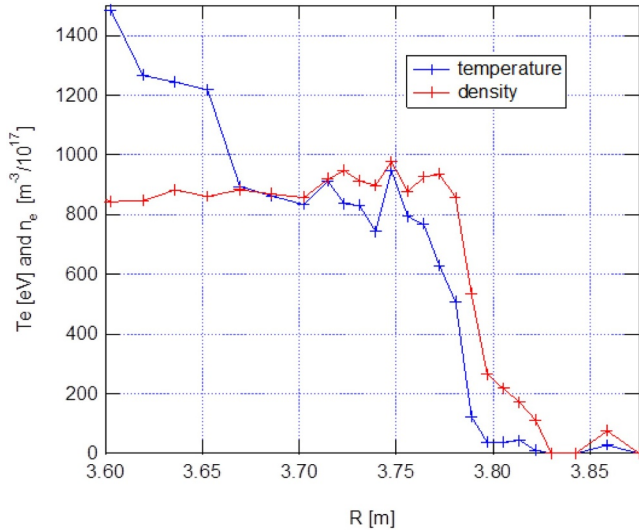

Fig. 2. KL9A lamella: (—) *N* + 2 (—) *N* + 1 (—) *N* (—) *N* − 1 (—) *N* − 2 and (—) standard KL9B. (a) Individual ELM heating as measured during the W-melting pulse (#91965, 38 ELMs in total). (b) Time evolution of the analysed ELM @ *t* = 12.048 s.

Fig. 3. HRTS density and temperature measurements as function of the plasma radius, before the ELM crash (t = 12.048 s).

the top of the pedestal $n_e = 9.10^{19}$ m^3 and $T_i = T_e = 800$ eV, yielding the ion Larmor radius $r_{Li} = 1.8$ mm for $B_T = 3.48$ T. A value which is close to the mean ion Larmor radius of a 50%/50% mixture of deuterium and tritium ions $r_{DT} = 2.0$ mm expected in ITER for the 15 MA burning reference scenario (assuming $T_i = 5000$ eV and $B_T = 6$ T on the outer vertical target) [16]. The protruding part of the sloped lamella ($h \approx 1.21$ mm) being smaller than two Larmor radii a decrease of the heat flux on the slope is expected because of ion is scrapped-off on the protruding W-lamella.

Fig. 4 shows, for the five lamellas in the field of view of the KL9A camera, a comparison of the deposited heat flux calculated by the three modelling (OA, PIC and IOC) assuming ambipolar parallel current flow ($q_{tot} = \frac{5}{7}q_i + \frac{2}{7}q_e$, with q_i and q_e the electron and ion heat fluxes) for the PIC and IOC calculations (floating surface condition). The deposited heat flux is reduced by a spatially averaged factor of ~33% and ~45%, with respect to OA (with no q_{BG}), for the IOC and PIC calculations, respectively. On the sloped lamella (N), the heat flux from the IOC calculation is higher than the PIC one. This discrepancy is attributed to the influence of the electric field and is in line with previous comparison of the two codes [17].
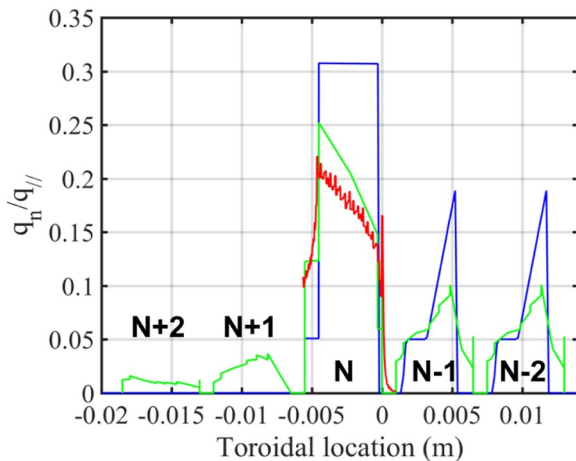

Fig. 4. Heat flux calculation along the curvilinear abscissa, normalize to $q_{||//}$ = 1 W/m^2. (—) OA, (—) PIC (with (—) q_i and (—) q_e) and (—) ion-orbit.

3.3. 3D thermal modelling and synthetic IR data

The 3D thermal modelling of the lamellas is performed with the finite element method (FEM) software ANSYS (V18.2). For the ELM analysis, in order to start the calculation with a realistic initial temperature field we used an equivalent heat flux, summing the inter-ELM and ELM heat load contribution, from the start of the pulse to the start of the ELM (at t = 12.048 s). The synthetics IR data are obtained by convoluting the temperature distributions with the modulated transfer function (MTF) of the instrument to simulate the spatial resolution related effects. The total MTF can be modelled by a Gaussian function in frequency space with σ being the standard deviation [9]. For the KL9A camera the pixel size and the standard deviation is determined from the thermal scene using the keyhole presence and the gap effect, we found $r \approx 0.85$ mm/pixel and $\sigma \approx 1$ mm equivalent to the value used for the L-mode analysis [10] when the pixel size was $r \approx 1.7$ mm.

Fig. 5 shows the calculated temperature distributions (in red), the synthetic IR data (in green) and the IR measurements (in black) in the poloidal (for the sloped lamella) and toroidal (for all lamellas) directions. This step is required to ensure realistic thermal condition of the all set of W-lamellas before the ELM impact. For the rest of the paper we will focus on the toroidal distribution of the surface temperature where the ELM heating is maximum, as shown in grey in the Fig. 5 (left). (For interpretation of the references to colour in this figure legend, the reader is referred to the web version of this article.)

4. Experimental results

4.1. Pure optical approximation (OA)

The ELM heat flux is first determined from the slope part of the special lamella. We found peak heat flux of $q_n \approx 384$ MW/m^2. Assuming no background heat flux $q_{BG} = 0$ MW/m^2 with Eq. (1), the corresponding parallel heat flux would be $q_{||}^{ELM} = 1250$ MW/m^2 (with $\alpha = 17.9°$). Fig. 6(a) shows a comparison between the IR data (black) and the synthetic IR data reconstructed with the transfer function of KL9A and $q_{||}^{ELM} = 1250$ MW/m^2 (purple) at the end of the ELM temperature rise. A good match is obtained on the sloped lamella (N) while important discrepancies are obtained on the other lamellas. The heating is clearly underestimated on the upstream lamellas ($N - 1$ and $N - 2$). About 150 °C is missing on the shaped lamellas, representing 40% of the measured heating for this ELM. To find a good agreement on the shaped lamellas ($N - 1$ and $N - 2$) we need to increase the parallel heat flux up to 2000 MW/m^2 during the ELM (blue line for the synthetic IR data) leading to have different parallel heat flux on the sloped and shaped lamellas which cannot be explained with physics arguments. With the pure OA we have no heating on the downstream lamellas as expected due to the magnetic shadowing of the sloped lamella.

A first solution would be to involve non parallel background heat flux as reported in [11]. The best match found on lamellas N, $N - 1$ and $N - 2$ is shown on Fig. 7 and corresponds to an ELM parallel heat flux $q_{||}^{ELM} = 1000$ MW/m^2 with an important background ELM heat flux $q_{BG} = 75$ MW/m^2 which is equal to 7.5% of the ELM parallel heat flux. Contrary to the observations done in COMPASS or TORE SUPRA [6,9] this level of background heat flux is too high to be attributed to local plasma radiation or charge exchange processes. Moreover with such ELM background heat flux, the heating on the shadowed lamellas ($N + 1$ and $N + 2$) would be overestimated by 90% (keeping in mind the fact that the apparent heating measured on these lamellas given by KL9A may be also overestimated with reflection effects due to the low tungsten emissivity). In the next section, we propose to investigate the finite Larmor radius effects associated with the energetic ELM as predicted by ion-orbit and PIC modelling [12].
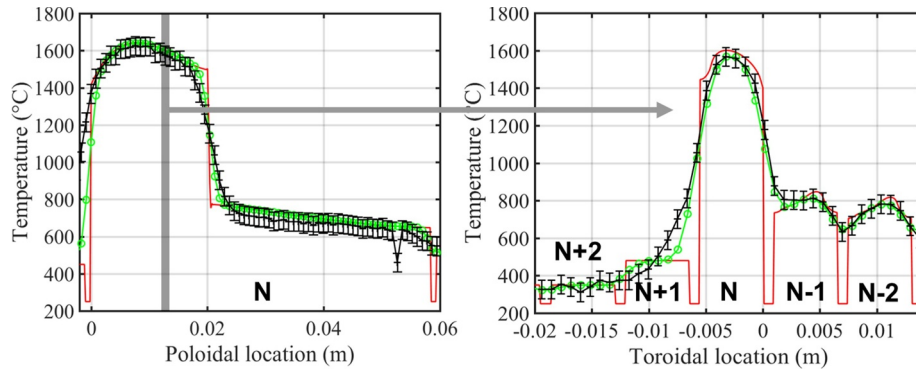
Fig. 5. (—) ANSYS, (—o—) synthetic IR data and (—+—) IR data. (left) poloidal and (right) toroidal temperature profiles @ $t = 12.048$ s before the ELM crash.
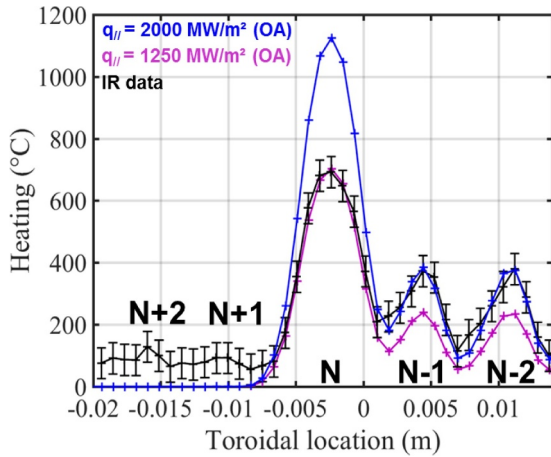

Fig. 6. Toroidal temperature profile for $q_{\parallel}^{ELM} = 1250$ MW/m² (—) synthetic IR data, for $q_{\parallel}^{ELM} = 2000$ MW/m² (—) synthetic IR data with $q_{BG} = 0$ MW/m² and (—) IR data.
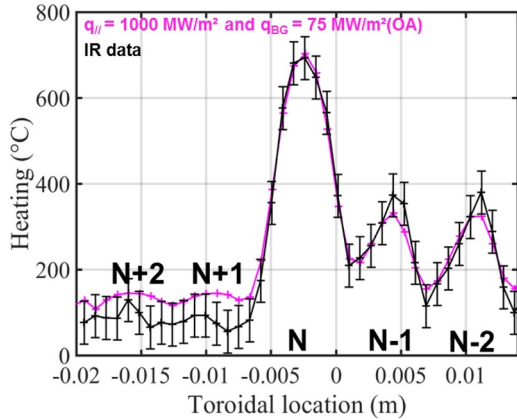

Fig. 7. Toroidal temperature profile for $q_{\parallel}^{ELM} = 1000$ MW/m² and $q_{BG} = 75$ MW/m², (—) synthetic IR data and (—) IR data.

4.2. PIC and ion-orbit modelling

Fig. 8 compares the OA (in blue with $q_{//\parallel}^{ELM} = 2000$ MW/m² and no q_{BG}), the IOC and the PIC calculations (with $q_{\parallel}^{ELM} = 2400$ MW/m² in green and red, respectively) to the IR measurements (in black). The OA calculation shows a good agreement on the shaped lamella but an important overheating of 435 °C (+63% of the measured heating) on the sloped lamella. The IOC calculation with $q_{\parallel}^{ELM} = 2400$ MW/m² keeps the good agreement on the shaped lamella and reduces the overheating on the sloped lamella to 275 °C (+40% of the measured heating) due to the

Larmor radius effect, as expected considering the heat flux shown in the Fig. 4.[1] A zoom over shaped lamella $N - 2$ shows that the overall heating distribution is also better caught with the IOC calculation by the consideration of the smoothing due to the ion Larmor radius. The PIC calculation performed on the sloped lamella (with flat W-lamellas around) reduces the overheating to 124 °C (+18% of the measured heating) due to the additional effect of the electric field. This level of discrepancy 18% becomes acceptable regarding the current hypothesis of the PIC simulation which is based on limited simulation box and limited physical processes (PIC modelling does not include plasma radiation and neutral particles coming from charge exchange, neither ionic reflection on the target leading to slight reduction of the plasma energy transfer to the target). Improved simulation box including upstream shaped W-lamella as well as more realistic plasma background (temperature, density and radiation) would be required to get better agreement.

5. Conclusion

ELM-induced transient melting has been successively achieved with regular Type-I ELMs during the W-melting experiment #91965 (3.25 MA/3.03 T with 27 MW input power). This discharge provides repetitive ELMs impacting two geometries, the round standard lamella and the protruding sloped lamella. Heating measured by the IR camera are compared with reconstructed synthetic data from 3D thermal modelling using heat loads derived from OA, IOC and PIC calculations. Results show that the ELM power deposition behaves differently than the optical projection of the parallel heat flux, contrary to the L-mode observations [10]. Using the same parallel heat flux with the pure optical approximation, it is impossible to reproduce the experimental IR data on both geometries. The modelling of the Larmor gyration, of the order of 1.8 mm here for deuterium ions, and self-consistent sheath electric field assuming floating conditions results in a net reduction of the heat load (~45% compared to OA) on the protruding 15° slope as observed experimentally. The comparison between experimental and synthetic IR data presented in this paper provides the first direct confirmation that these two effects, ion Larmor radius and sheath electric field, do occur during the Type-I ELM crashes. These effects must therefore be considered in order to simulate the material redistribution after ELM-induced transient melting,. Further improvement would require the extension of the PIC simulation box (including the upstream shaped W-lamella), as well as improved plasma wall interaction modelling (temperature, density, plasma radiation and ionic reflection on the wall).

---

[1] The difference of $q_{\parallel}^{ELM}$ required to have good agreement on the shaped lamella between OA and IOC calculations (2000 vs 2400 MW/m², respectively) is explained by the heat flux smoothing in the toroidal direction with the IOC calculation due to the Larmor radius effect, we need higher $q_{\parallel}^{ELM}$ to find the same maximal heating on the shaped lamellas.

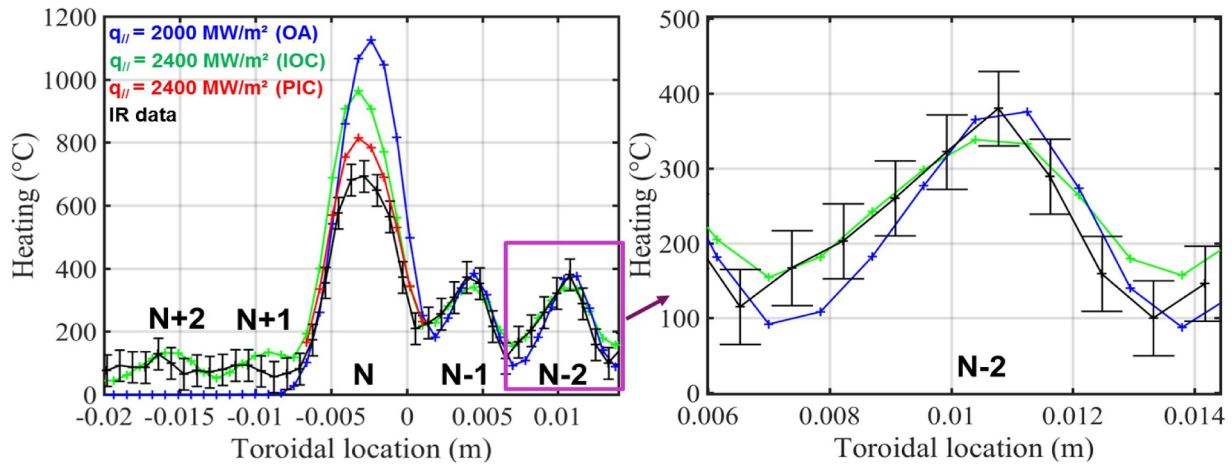**Fig. 8.** Toroidal temperature profile for $q_\parallel^{ELM} = 2000\,MW/m^2$ (—) synthetic IR data OA with $q_{BG} = 0\,MW/m^2$, for $q_\parallel^{ELM} = 2400\,MW/m^2$, (—) synthetic IR data PIC, (—) synthetic IR data IOC, and (—) IR data.

Acknowledgements

References

[1] R.A. Pitts, et al., Nucl. Mater. Energy 0 (2017) 1–15.
[2] J.W. Coenen, et al., J. Nucl. Mater. 463 (2015) 78–84.
[3] J.W. Coenen, et al., Nucl. Fusion 55 (2015) 023010.
[4] J.W. Coenen, et al., Phys. Scr. T170 (2017) 0140139pp.
[5] K. Krieger, et al., Nucl. Fusion 58 (2018) 026024.
[6] R. Dejarnac, et al., Nucl. Fusion 58 (2018) 066003.
[7] S.H. Hong, et al., Nucl. Mater. Energy 12 (2017) 1122–1129.
[8] R.E. Nygren, Bull. Am. Phys. Soc. 60 (19) (2015).
[9] Y. Corre, et al., Nucl. Fusion 57 (2017) 016009.
[10] Y. Corre, et al., Nucl. Fusion 57 (2017) 066009.
[11] D. Iglesias et al. Accepted in NF (2018).
[12] R. Dejarnac, et al., Nucl. Fusion 54 (2014) 123011.
[13] P. Mertens, et al., Fusion Eng. Des. 84 (2009) 1289–1293.
[14] I. Balboa, et al., Rev. Sci. Instrum. 83 (2012) 10D530.
[15] R. Dejarnac, J.P. Gunn, J. Nucl. Mater. 363-5 (2007) 560–564.
[16] J.P. Gunn, et al., Nucl. Fusion 57 (2017) 046025.
[17] M. Komm, et al., Nucl. Fusion 57 (2017) 126047.